

## Chromospheric Heating by Acoustic Waves Compared to Radiative Cooling: II – Revised Grid of Models

VAHID ABBASVAND,<sup>1,2</sup> MICHAL SOBOTKA,<sup>1</sup> PETR HEINZEL,<sup>1</sup> MICHAL ŠVANDA,<sup>1,2</sup> JAN JURČÁK,<sup>1</sup> DARIO DEL MORO,<sup>3</sup>  
FRANCESCO BERRILLI,<sup>3</sup>

<sup>1</sup>*Astronomical Institute of the Czech Academy of Sciences (v.v.i.)  
Fričova 298, 25165 Ondřejov, Czech Republic*

<sup>2</sup>*Astronomical Institute of Charles University, Faculty of Mathematics and Physics  
V Holešovičkách 2, 180 00 Praha 8, Czech Republic*

<sup>3</sup>*Department of Physics, University of Roma Tor Vergata  
Via della Ricerca Scientifica 1, I-00133 Rome, Italy*

(Received October 22, 2019; Revised December 12, 2019; Accepted December 29, 2019)

Submitted to ApJ

### ABSTRACT

Acoustic and magnetoacoustic waves are considered to be possible agents of chromospheric heating. We present a comparison of deposited acoustic energy flux with total integrated radiative losses in the middle chromosphere of the quiet Sun and a weak plage. The comparison is based on a consistent set of high-resolution observations acquired by the IBIS instrument in the Ca II 854.2 nm line. The deposited acoustic-flux energy is derived from Doppler velocities observed in the line core and a set of 1737 non-LTE 1D hydrostatic semi-empirical models, which also provide the radiative losses. The models are obtained by scaling the temperature and column mass of five initial models VAL B–F to get the best fit of synthetic to observed profiles. We find that the deposited acoustic-flux energy in the quiet-Sun chromosphere balances 30–50 % of the energy released by radiation. In the plage, it contributes by 50–60 % in locations with vertical magnetic field and 70–90 % in regions where the magnetic field is inclined more than 50° to the solar surface normal.

*Keywords:* Sun: chromosphere — Sun: faculae, plages — Sun: oscillations

### 1. INTRODUCTION

The energy released by radiation from the solar chromosphere is mostly concentrated in the strong lines of Ca II, Mg II, and hydrogen Lyman- $\alpha$  as well as in the H<sup>-</sup> continuum (Vernazza et al. 1981). It is characterized by net radiative cooling rates (radiative losses). The estimate of the total radiative losses integrated over the height of the chromosphere is 4300 W m<sup>-2</sup> in the quiet Sun (Avrett 1981) and it is by a factor of 2 to 4 higher in active regions (Withbroe & Noyes 1977). This radiative cooling must be balanced by heating processes that deliver energy to the chromosphere. The dominant process heating the upper layers of the solar atmosphere is still being intensively debated. There are many agents

considered by various studies (see Jess et al. 2015, for a review), which could be grouped into two fundamentally different classes: (1) Mechanisms that are usually connected with heat releases during the reconnection processes in the magnetic field and (2) mechanisms that are associated with the deposit of energy by various kinds of waves. In the present work, we focus on the latter class.

Waves are generated near the solar surface by turbulent motions of the convective plasma and propagate upwards, where they can dissipate a considerable part of their energy in the chromosphere. In the magnetized solar atmosphere, there exist three principal types of MHD waves: Alfvén waves as well as fast and slow magnetoacoustic waves (Khomenko 2009; Khomenko & Cally 2012). These waves with magnetic component are considered extremely important. Low-frequency waves may represent a significant source of energy, related to

the so-called magnetic portals (Jefferies et al. 2006) or to magnetoacoustic-gravity waves (Jefferies et al. 2019). These waves are generally not allowed to propagate higher into the atmosphere because their frequency does not exceed the expected photospheric cutoff frequency 5.2 mHz (Bel & Leroy 1977). However, in regions where the photospheric magnetic field is inclined with respect to the gravity vector, the cutoff frequency can be lowered by means of the ramp effect (Stangalini et al. 2011). This allows waves with frequencies far below 5.2 mHz, which would otherwise be trapped in the photosphere, to propagate into the upper atmosphere. Recently, Rajaguru et al. (2019) used *Solar Dynamics Observatory* (Pesnell et al. 2012) data to discuss thoroughly the relations between magnetic field properties and the propagation of acoustic waves.

Sobotka et al. (2016, hereafter Paper I) studied the hypothesis of chromospheric heating by acoustic and magnetoacoustic waves. This work was based on 70-minute long observations of the Ca II 854.2 nm near-infrared line with the *Interferometric Bidimensional Spectrometer* (IBIS, Cavallini 2006) at the *Dunn Solar Telescope*. Sequences of Dopplergrams were used to compute energy flux carried by (magneto)acoustic waves and a simplistic grid of seven semi-empirical non-LTE (that is, with departures from the local thermodynamic equilibrium, LTE) hydrostatic models of the atmosphere to estimate the radiative losses. Although the propagation and dissipation of waves in the chromosphere is generally a time-dependent process, 1D static models are still a reasonable tool to represent time-averaged physical conditions in long-lived structures of the solar atmosphere (Heinzel & Štěpán 2019). In Paper I we found that a significant portion of the radiative losses could be replenished by the dissipative acoustic flux generated by the  $p$ -modes, which were converted to magnetoacoustic modes in the inclined magnetic field. We have shown that there was a correlation between the estimate of the acoustic flux dissipation in the region and the estimate of the radiative losses. That provided an indication that there indeed was a contribution of the acoustic waves to the heating of the chromosphere, which should be considered.

A weak point of that work was a scarce grid of only seven atmospheric models, which were used to calculate the radiative cooling rates as well as the acoustic fluxes. In this paper we present an analysis of the same observations as in Paper I, applying a much finer grid of models obtained by up- and downscaling the frequently used semi-empirical models of Vernazza et al. (1981, VAL models), to make sure that the comparison

**Table 1.** Parameters of the IBIS data set

Date and time	2008 October 15, 16:34 – 17:44 UT
Scanned lines	Fe I 617.33 nm ( $I, Q, U, V$ ); Ca II 854.2 nm ( $I$ )
No. of sp. points	21 in each line
Wavelength spacing	2 pm (Fe I); 6 pm (Ca II)
Field of view	$38''0 \times 71''5$ ; part of NOAA 11005
Region of interest	$13''7 \times 39''7$
Pixel size	$0''167 \times 0''167$
Spatial resolution	$0''4$ (Sobotka et al. 2012)
Exposure time	80 ms
Spectral scan time	52 s (time resolution)
No. of sp. scans	80

of deposited acoustic flux and radiative losses is more conclusive.

## 2. OBSERVATIONS AND DATA ANALYSIS

The target, a slowly decaying bipolar active region NOAA 11005 located at 25.2 N and 10.0 W (heliocentric angle  $\vartheta = 23^\circ$ ) was observed with IBIS on 2008 October 15 from 16:34 to 17:44 UT. A pore surrounded by a superpenumbra (Sobotka et al. 2013) was present in the leading part of the region. A weak chromospheric plage with equal polarity was located near the pore (see Figure 1 in Paper I). The IBIS data set was described in detail in Sobotka et al. (2012), Sobotka et al. (2013), and Paper I. Two spectral lines, Ca II 854.2 nm (intensity only) and Fe I 617.33 nm (full Stokes vector) were observed simultaneously. The relevant parameters for both spectral lines are summarized in Table 1.

The data-processing procedures were described thoroughly by Sobotka et al. (2012) and Sobotka et al. (2013). We concentrated on the region of interest (ROI)  $13''7 \times 39''7$  ( $82 \times 238$  pixels) that included the plage eastward of the pore and a quiet-Sun region. The location of ROI in the whole field of view is shown in Figure 1 of Paper I. The following observables were obtained from the IBIS data set (see Paper I for details):

(1) The magnetic-field vector in the photosphere, retrieved from the full-Stokes spectral scan of Fe I 617.33 nm taken at 17:10 UT by means of the Stokes inversion code based on response functions (SIR, Ruiz Cobo & del Toro Iniesta 1992). Because the acoustic flux in the chromosphere is very sensitive to the inclination of magnetic field to the solar surface normal, we revise the calculations of Paper I to avoid uncertainties in regions with weak fields, where the Stokes  $Q$ ,  $U$ , and  $V$  signals are dominated by noise. In such cases, the code returns an unreliable line-of-sight (LOS) inclination near

90° (transversal direction), which can be removed by a mask that for the fields weaker than 350 G sets to zero all inclination angles in the range  $\pm 5^\circ$  from the transversal direction. We update the method of removing the 180° ambiguity of the LOS azimuth, using the AMBIG code (Leka et al. 2009). In the revised calculations, we also removed a bug in the transformation from the LOS reference frame to the local reference frame (LRF) that led to an overestimation of magnetic inclination in the plane. We use routines from the AZAM code (Lites et al. 1995) for the transformation from the LOS reference frame to LRF.

(2) Time-dependent line-of-sight velocities, measured in the inner wings of the Ca II 854.2 nm core at  $\pm 18$  pm and in the line center. According to Cauzzi et al. (2008), the inner wings are formed at approximately 900–1000 km above the optical depth  $\tau_{500} = 1$  and the line centre at 1400–1500 km. These velocities are used to calculate power spectra of oscillations in two different layers of the chromosphere.

(3) Mean profiles of the Ca II 854.2 nm line, obtained by time-averaging over the 70-minute observing period of the observed profiles with removed Doppler shifts. They are used to find the most appropriate semi-empirical models at each location in ROI.

The cadence of scans (52 s) and the length of the time-series sets the maximum detectable frequency of oscillations to 9.6 mHz and the frequency resolution to 0.24 mHz, suitable to analyze low-frequency waves. Power spectra of the line-of-sight velocities were calculated using the standard Fourier analysis and the results were discussed in Sobotka et al. (2013). The acoustic energy fluxes at the heights of 900 km and 1500 km were estimated following Bello González et al. (2009). The method consists in an integration over frequencies of the product of gas density, spectral power density, and group velocity of energy transport. The frequency integration range spans between the acoustic cutoff frequency and the maximum detected frequency—see Paper I for details. The quantities depend on the gas density and pressure at the given height, which are taken from the model atmosphere. The acoustic cutoff frequency is proportional to the cosine of the magnetic field inclination to the solar surface normal.

Taking into account that the acoustic flux estimated at 900 km approximates the incoming energy flux that may partly dissipate in the atmosphere, while the acoustic flux at 1500 km corresponds to the energy flux that has passed without dissipation, then the deposited acoustic flux in the chromospheric layers between 900 km and 1500 km is the difference between these two fluxes. The

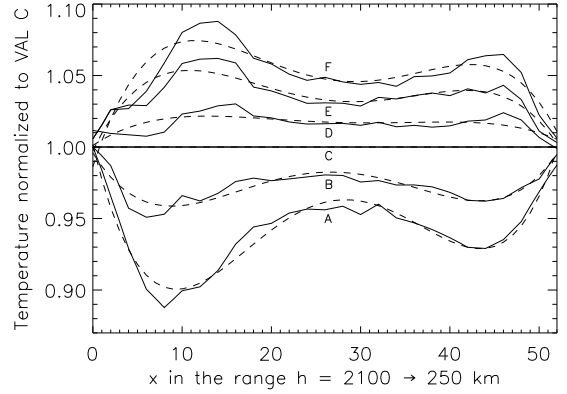


**Figure 1.** Temperature stratifications of models VAL A–F normalized to VAL C (solid lines) in the range  $h$  from 2100 km to 250 km. Dashed lines show the approximation by fourth-order polynomials.

corresponding net radiative cooling rates are integrated in the same range of heights.

### 3. GRID OF CHROMOSPHERIC MODELS

The grid of models has been constructed keeping the number of free parameters as low as possible. We scale the existing set of semi-empirical 1D hydrostatic models VAL A–F, which describe the solar atmosphere from intranetwork to bright network features, by changing independently the temperature and column mass stratifications. Adopting the column mass as an independent variable makes it possible to conserve the condition of hydrostatic equilibrium in the scaled models.

The original VAL models specify the column mass  $m$ , optical depth  $\tau_{500}$  at 500 nm, temperature  $T$ , microturbulent velocity  $v_t$ , hydrogen density  $n_H$ , electron density  $n_e$ , total pressure  $P_{\text{tot}}$ , gas pressure to total pressure ratio  $P_g/P_{\text{tot}}$ , and density  $\rho$  in 52 geometrical heights  $h$  ranging from  $-75$  km to 2400–2700 km ( $h = 0$  is at  $\tau_{500} = 1$ ). The microturbulence stratification is practically equal in all models A–F at the heights from  $-75$  km to 2000 km, that is, in the whole photosphere and chromosphere, and it is not changed in scaled models. To improve numerical accuracy of the following computations, we resampled the models to 103 heights by means of the linear interpolation. The scaling of these initial models is done in two steps: (1)  $m$  and  $T$  stratifications are changed and (2) the other model quantities are recalculated.

We can find an adequate way to change  $m$  and  $T$  by adopting, for example, the VAL C model as the initial one and reproducing the stratifications of all the other VAL models. In general, the scaling algorithm must be able to reproduce all the stratifications using any VAL

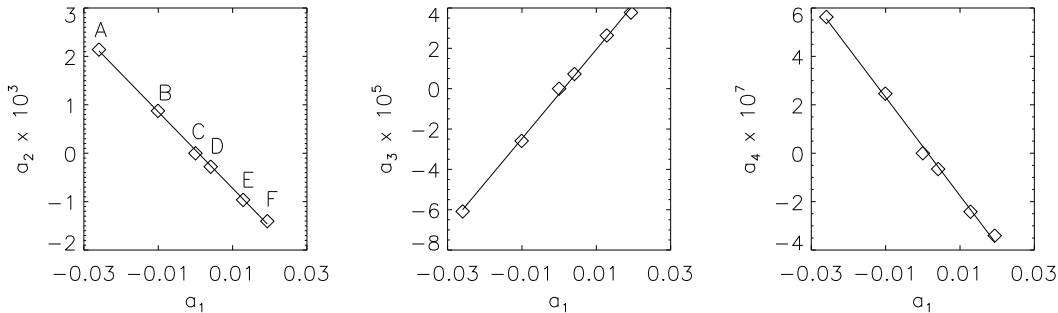


**Figure 2.** Linear relations of the fourth-order polynomial coefficients  $a_{1-4}$  of the temperature scaling. Diamonds show values corresponding to the models VAL A–F.

model as the initial one. The following solution was adopted: The initial column mass stratification  $m_0(h)$  is changed for  $h \geq 450$  km ( $m < 0.1$  g cm $^{-2}$ ) whereas it is kept unchanged in deeper layers. The changes are controlled by scaling parameter  $p_m$ , so that the scaled column mass is

$$\begin{aligned}
 m_x &= b_x m_{0x}, \text{ where} \\
 b_x &= p_m \text{ for } h \geq 2000 \text{ km,} \\
 b_x &= p_m + (1 - p_m) x / (x_{450} - x_{2000}) \\
 &\text{for } 2000 \text{ km} > h \geq 450 \text{ km,}
 \end{aligned}$$

and  $x$  is the sampling (row) index in the model table. In upper layers, from the maximum height down to  $h \approx 2000$  km,  $b_x$  is simply a multiplicative factor equal to  $p_m$ . In deeper layers ( $h < 2000$  km), this factor linearly decreases or increases to reach unity at  $h \approx 450$  km.

The initial temperature stratification is changed in the range of heights from approximately 250 km to 2100 km; the upper and lower parts remain equal to the initial model. To derive the scaling parameter  $p_T$ , we normalize the temperature stratifications  $T_x$  of all VAL models to VAL C:  $A_x = T_x / T_{x \text{ VAL C}}$ . These normalized stratifications can be approximated by a fourth-order polynomial in the form  $A'(x) = 1 + \sum_{i=1}^4 a_i x^i$  (Figure 1). The coefficients  $a_i$  are mutually dependent and  $a_{2-4}$  can be expressed by multiples of  $a_1$  (Figure 2), particularly,  $a_{i=2,3,4} = a_1 q_i$ , where  $q_i = [-7.90 \cdot 10^{-2}, 2.21 \cdot 10^{-3}, -2.03 \cdot 10^{-5}]$ . The values of  $q_i$  are practically independent of the initial model. Thus,  $a_1$  can be used as the temperature scaling parameter,  $p_T = a_1$ . The scaled temperature stratification (in the range 250–2100 km) is then calculated as

$$T_x = T_{0x} (1 + p_T x + p_T \sum_{i=2}^4 q_i x^i),$$

where  $T_{0x}$  are the initial temperatures.

For each of the initial models VAL we calculated a grid of 2806 scaled models using a combination

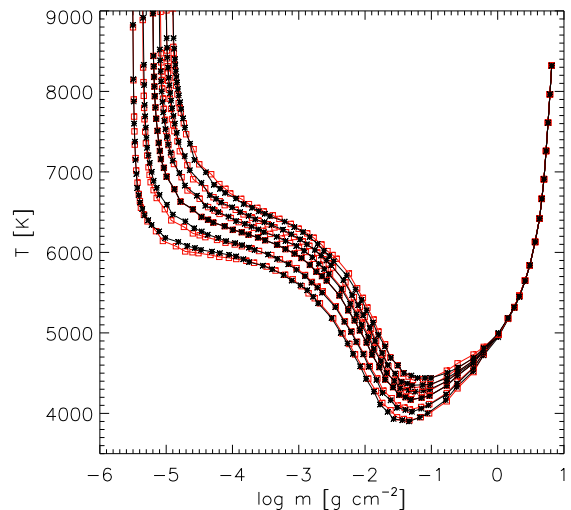


**Figure 3.** Temperature versus column mass plots of the VAL A–F models scaled from the model C. Red and black lines show the scaling results and the original VAL models, respectively. The symbols denote sampling of the models.

of the parameters  $p_m = [0.5, 0.6, \dots, 4.9, 5.0]$  and  $p_T = [-0.030, -0.029, \dots, 0.029, 0.030]$ . In Figure 3 we show that the models VAL A–F can be reproduced by scaling the model C, applying the sets of parameters  $p_m = [0.5, 0.7, 1.0, 1.3, 1.6, 2.0]$  and  $p_T = [-0.021, -0.010, 0.000, 0.006, 0.012, 0.020]$ , respectively. In total, we have 16836 models in the grid parametrized by  $p_m$ ,  $p_T$ , and the initial model selection.

The models, which have been obtained by varying the temperature structure on the column-mass scale, are used as the input atmospheres in the non-LTE radiative-transfer codes MALI. MALI stands for the Multi-level Accelerated Lambda Iterations technique with preconditioning of the statistical-equilibrium equations according to Rybicki & Hummer (1991, 1992). The density structure is obtained from the hydrostatic equilibrium for a given temperature structure and the radiative transfer

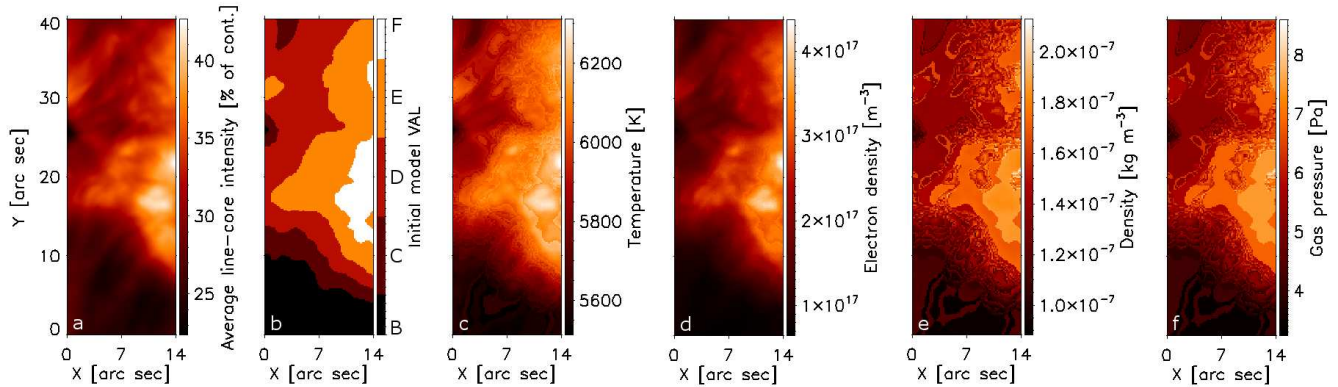


**Figure 4.** Maps of (a) Ca II 854.2 nm line-core intensity, (b) selection of initial models, (c) temperature, (d) electron density, (e) density, and (f) gas pressure. The maps (c–f) are retrieved from resulting scaled models at  $h = 900$  km.

equation is solved in a semi-infinite atmosphere subject to standard boundary conditions. First we solve the hydrogen problem using a 5-level plus continuum atomic model. To obtain the gas density, we add the helium but we neglect the helium ionization in computing the electron density within the atmosphere. For hydrogen resonance lines Lyman- $\alpha$  and Lyman- $\beta$  we consider the standard angle-averaged partial frequency redistribution (PRD) for the scattering part of the source function and all other lines are treated in the complete redistribution.

The microturbulence, taken from the initial VAL model, is consistently included in the hydrostatic equilibrium as the turbulent pressure and it enters also in the line broadening calculations. The resulting electron densities are then used, together with the temperature structure, in the Ca II version of the MALI code, which solves the non-LTE problem for a 5-level plus continuum model of Ca II–Ca III ions. This governs the Ca II H and K resonance lines, the Ca II infrared triplet lines and the five continua. Again, PRD is used for both resonance lines H and K. We perform detailed synthesis of the Ca II 854.2 nm line, using all relevant broadening mechanisms. Due to uncertainties in the Van der Waals damping parameter, we adjust it in order to better fit the wings of this line. From the grid of models we compute the synthetic line profiles of the 854.2 nm line and use them to find the best fit to the observed profiles (see Section 4) at all positions in ROI.

The energy losses due to radiation are characterized by the net radiative cooling rates or simply the net radiative losses. For selected best-fit models, at each position in ROI and model height, we finally compute the net radiative cooling rates due to hydrogen, Ca II, and Mg II. These are the main contributors in the solar chromosphere as demonstrated in Vernazza et al. (1981). The Mg II version of our MALI code uses a 5-level plus continuum Mg II–Mg III atomic model and treats the two

resonance lines Mg II h and k and the triplet lines. Both resonance lines are again computed using the PRD approach. Contrary to optically-thin losses from the solar corona, the chromospheric losses in the above listed lines must be computed by solving the complex non-LTE radiative transfer problem, because these lines are optically thick and there is no simple and sufficiently precise prescription for an easy estimate of such losses. The resulting net radiative losses are then integrated along the atmospheric height in the range from 900 km to 1500 km, which corresponds to the range where the measured acoustic energy flux is dissipated (see Section 2). At such heights, the losses are dominated by Ca II lines with some contribution of Mg II lines h and k and hydrogen continua. A strong coolant is the hydrogen Lyman- $\alpha$  line, but this is formed higher in the atmosphere close to the transition zone and thus does not enter our integration over the heights of interest.

#### 4. DEPOSITED ACOUSTIC FLUX COMPARED TO RADIATIVE COOLING

The initial models VAL B–F were assigned to different areas in ROI in accordance with the brightness of the Ca II 854.2 nm line core (Figures 4a and b). Then, a scaled model from the grid, which provided the best match of the synthetic  $I_{\lambda}^{\text{syn}}$  to the local mean observed profile  $I_{\lambda}^{\text{obs}}$  of the line, was assigned to each of 19516 positions in ROI. The models have been found by minimizing the merit function

$$\chi^2(\text{model}) = \sum_{\lambda} [I_{\lambda}^{\text{syn}}(\text{model}) - I_{\lambda}^{\text{obs}}]^2.$$

In total, 1737 different models were used. The retrieved values of model  $T$ ,  $n_e$ ,  $\rho$ , and  $P_g$  at the geometrical height  $h = 900$  km are shown in Figures 4c–f. Because each position in ROI is characterized by a 1D model unrelated to its surroundings, the maps of  $\rho$ , and  $P_g$

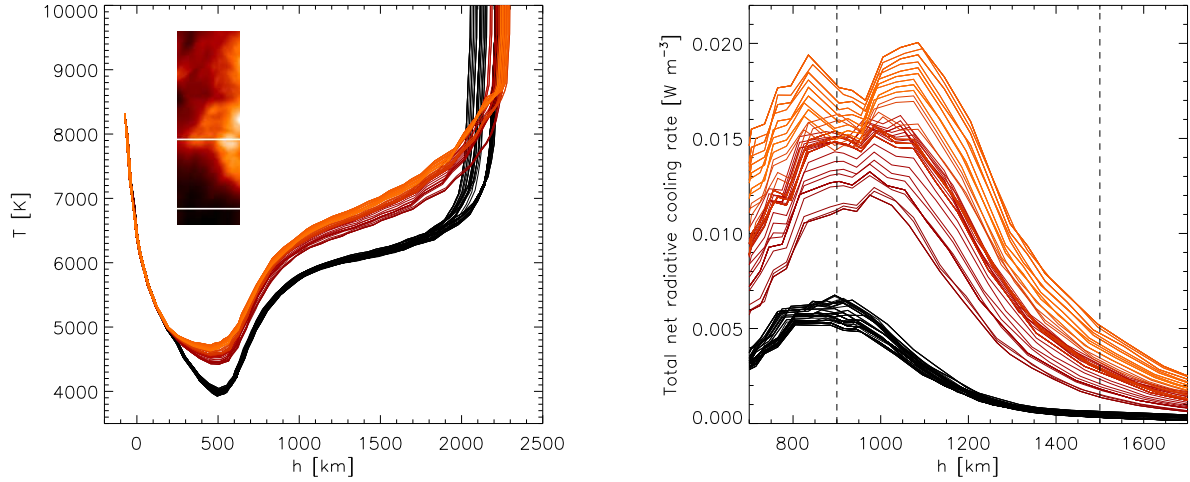


**Figure 5.** Left: Examples of quiet-Sun temperature stratifications with height (black) at positions along the bottom white line in the inset image of the line-core intensity. Red-to-orange temperature curves correspond to positions from left to right along the top white line that crosses the plage. Right: Total net radiative cooling rates versus height in quiet Sun (black) and plage (red-orange) at the same positions. Vertical dashed lines delimit the integration range.

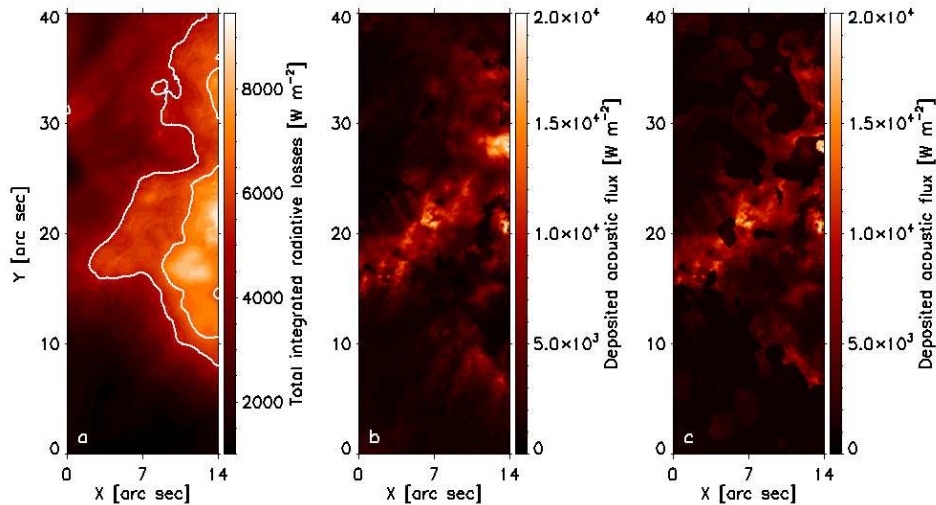


**Figure 6.** (a) The total integrated radiative losses map with contours of 5000 and 6500  $\text{W m}^{-2}$ . The deposited acoustic flux maps are calculated using (b) the original magnetic inclination angles and (c) the corrected ones.

have a noisy appearance. The local differences, however, are small—for example, the standard deviation of gas pressure in the “noisy” subfield  $6'' < x < 11''$ ,  $30'' < y < 40''$  is 0.5 Pa (9 % of the mean value). Examples of typical temperature stratifications in quiet-Sun and plage are depicted in the left panel of Figure 5. The inset image of the Ca II 854.2 nm line core intensity shows positions of the examples: the quiet-Sun temperatures (black curves) correspond to the bottom white line, while those in the plage are taken along the top white line and the colors of the temperature curves change from dark red to orange moving from left to right.

The total net radiative cooling rates (a sum of the Ca II, Mg II, and H contributions) are calculated for each model in ROI and integrated over the height range 900–1500 km. The right panel of Figure 5 shows examples of the height dependence of cooling rates in the quiet Sun and plage at the same positions as of the temperature stratifications. In the plage, the total cooling rates have a maximum at  $h = 1000$ – $1100$  km, which corresponds to maximum cooling rates of Ca II (the Mg II contribution is by an order lower). A secondary peak, caused by enhanced contribution of H and H<sup>-</sup> continua in hot and dense atmospheres, appears around

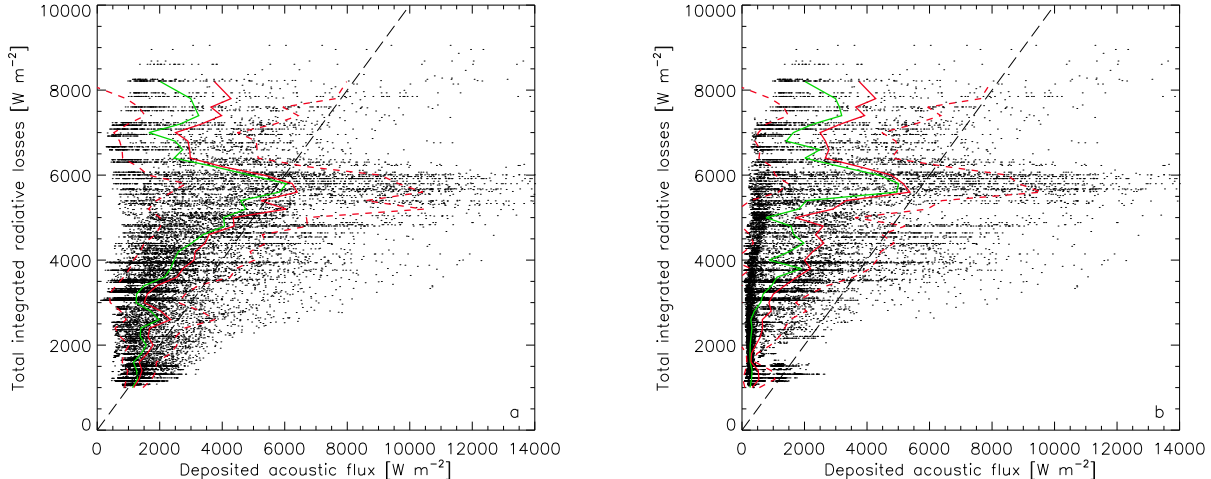


**Figure 7.** Scatter plots of total integrated radiative losses versus deposited acoustic flux in the region of interest (19516 points). The acoustic fluxes are calculated using (a) the original magnetic inclination angles and (b) the corrected ones. Solid lines show average (red) and median (green) values together with red dashed lines of  $\pm 1\sigma$ . The straight dashed line represents the full balance of radiative losses by acoustic flux deposit.

$h = 800$  km in the brightest part of the plage (orange curves). It does not enter our integration range. The map of the total integrated radiative losses is depicted in Figure 6a.

We calculate the deposited acoustic fluxes (see Section 2) using two different sets of magnetic field inclinations to estimate the influence of uncertainties in the inclination angle: (i) Original inclination angles retrieved from the inversion, including the unreliable values near  $90^\circ$  in weak-field or non-magnetic regions. The resulting map of the deposited acoustic flux is shown in Figure 6b. (ii) Corrected inclination angles, where the unreliable values are set to zero by means of the mask described in Section 2. The corresponding deposited acoustic flux map is shown in Figure 6c. The coefficient of spatial correlation between the total integrated radiative losses and the deposited acoustic flux is 0.47 in the case of (i) and 0.50 in the case of (ii).

Scatter plots of total integrated radiative losses  $L$  versus the acoustic energy flux  $\Delta F_{ac}$  deposited in the chromosphere between  $h = 900$  and  $1500$  km are shown in Figure 7a and b for the original inclination angles and the corrected ones, respectively. The red solid line represents mean values of  $\Delta F_{ac}$  that fall into  $200 \text{ W m}^{-2}$  wide bins of the  $L$  histogram. The bins must contain at least 100 points to calculate the mean value. Likewise, the green line represents median values. The red dashed lines delimit the  $\pm 1\sigma$  range that characterizes the scatter of individual points in each bin. When the unreliable horizontal magnetic inclination is included (Figure 7a), the deposited acoustic fluxes in the quiet-Sun area ( $L < 5000 \text{ W m}^{-2}$ ) almost double those calcu-

lated using the corrected inclination values (Figure 7b). This is not realistic because of too many points where  $\Delta F_{ac} > L$ . The increase of  $\Delta F_{ac}$  is much smaller in the plage, where the magnetic inclination is determined reliably. In the further discussion, we shall use the deposited acoustic fluxes calculated using the corrected inclination angles.

For most of the points (88 %) in the plot (Figure 7b),  $L > \Delta F_{ac}$ , that is, the deposited acoustic flux is insufficient to balance the radiative losses and maintain the (semi-empirical) temperature at corresponding positions in ROI. The scatter of  $\Delta F_{ac}$  versus  $L$  is large, so that we have to express the contribution of the deposited acoustic flux to the radiative losses statistically, using the ratios  $\overline{\Delta F_{ac}}/\overline{L}$  and  $\text{median}(\Delta F_{ac})/\overline{L}$ . Their values start at 0.3 (median 0.2) for  $L < 3500 \text{ W m}^{-2}$  and increase to 0.5 (median 0.3) for  $3500 < L < 5000 \text{ W m}^{-2}$  in the quiet area. They reach 0.7 (median 0.6) with a peak of 0.9 for  $5000 < L < 6500 \text{ W m}^{-2}$  at the periphery of the plage, where the magnetic inclination is large, and drop to 0.5 (median 0.4) for  $L > 6500 \text{ W m}^{-2}$  in the brightest part of the plage with the nearly vertical magnetic field. The points with  $L < \Delta F_{ac}$  will be discussed in Section 5.

Compared to the results of Paper I, the median values of  $\Delta F_{ac}$  are consistent excepting the brightest parts of the plage ( $L > 6500 \text{ W m}^{-2}$ ), where the magnetic inclination was overestimated. Moreover, the revision of the magnetic inclination map resulted in an increase of  $\Delta F_{ac}$  at the plage periphery ( $L \simeq 6000 \text{ W m}^{-2}$ ). Other differences can be explained by improved values of the gas density, to which the acoustic fluxes are directly pro-

portional. The present set of 1737 atmospheric models provides a more realistic density distribution than the simple grid of only seven models.

## 5. DISCUSSION AND CONCLUSIONS

A quantitative comparison of deposited acoustic energy flux with total integrated radiative losses in the middle chromosphere of the quiet Sun and a weak plage is made. The comparison is based on a consistent set of high-resolution observations acquired by the IBIS instrument in the line Ca II 854.2 nm. The deposited acoustic flux is derived from Doppler velocities observed in the line core and a set of 1737 non-LTE 1D hydrostatic semi-empirical models, which are also used for the calculation of radiative losses. The models are obtained by scaling the temperature and column mass of five initial models VAL B–F (Vernazza et al. 1981) to get the best fit of synthetic to time-averaged observed profiles of the Ca II 854.2 nm line.

The fit quality  $\chi_{\min}^2$  changes with the position in ROI. We define the bad-fit areas where  $\chi_{\min}^2$  is larger than  $2\sigma$  of its statistical distribution. Several of them, where the observed profiles are broader than the synthetic ones, coincide with regions of enhanced magnetic field in the pore and plage. Contours that outline the bad-fit areas together with the map of magnetic-field strength are shown in Figure 8a. The Zeeman broadening of the Ca II line with Landé factor  $g = 1.1$  probably does not play a major role. Rather, this effect might be explained by the fact that our 1D semi-empirical models do not account for the complex 3D distribution of thermodynamic and magnetic parameters in such areas. The bad-fit areas represent 12.5 % of the data set and a mask is made to remove the affected points from the scatter plot of  $L$  versus  $\Delta F_{\text{ac}}$ . This removal alters the plot shown in Figure 7b and the derived statistical values only in the part of  $L > 6500 \text{ W m}^{-2}$ , corresponding to the brightest plage region, where  $\overline{\Delta F_{\text{ac}}}$  becomes larger by the factor of 1.3 on average and its contribution to the total integrated radiative losses  $\overline{\Delta F_{\text{ac}}}/\overline{L}$  increases from 0.5 to 0.6.

In 12 % points of our data set, the deposited acoustic energy flux is larger than the total integrated radiative losses ( $L < \Delta F_{\text{ac}}$ ). Regions formed by these points are shown in Figure 8b together with the bad-fit ones in white and black colors, respectively. The  $L < \Delta F_{\text{ac}}$  regions appear at locations where **the magnetic inclination is larger than  $60^\circ$**  and temporal variations of Doppler velocity and intensity of the Ca II 854.2 nm core are strong (cf. Figure 1 and its animation in Paper I): around the border between the pore’s superpenumbra

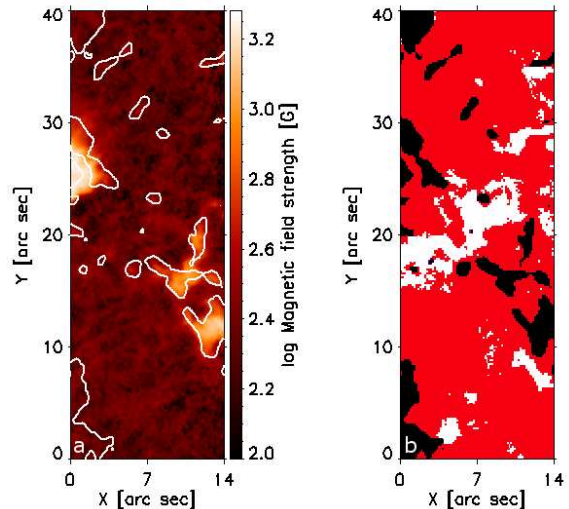


**Figure 8.** (a) Map of magnetic field strength (in logarithmic scale) with contours of areas where the fit of synthetic to observed Ca II line profiles is worse than  $2\sigma$ . (b) Areas of radiative losses smaller than the deposited acoustic flux (white) together with the bad-fit areas (black).

and plage (subfield  $0'' < x < 10''$ ,  $15'' < y < 25''$ ) and partly at the periphery of the plage.

We have shown that the deposited acoustic-flux energy in the quiet-Sun chromosphere balances 30–50 % of the energy released by radiative losses. The energy carried by (magneto)acoustic waves in the plage supplies 50–60 % of the radiated energy at locations with vertical magnetic field and 70–90 % in regions where the magnetic field is inclined more than  $50^\circ$ . These values are statistical averages of results with a large individual scatter and they are based on one observation of a single small solar area. They are also critically sensitive to the correct determination of the magnetic field inclination, particularly in the quiet-Sun region. We also have to note that the area considered as quiet Sun in our ROI is close to the plage and it falls within the extended canopy region of the plage’s magnetic field (see Figure 1 in Paper I). The effect of “magnetic shadows”, which are related to the elevated magnetic field forming the Ca II fibrils (Vecchio et al. 2007), reduces the oscillatory power in this region, as seen from the power maps in Figure 7 of Sobotka et al. (2013). Consequently, the deposited acoustic flux in our “quiet area” may be lower than that in quiet regions far from the plage. Additional studies of different quiet and active regions in various chromospheric lines together with precise measurements of magnetic field inclination are needed to obtain more general and conclusive results.

## ACKNOWLEDGMENTS

We thank the anonymous reviewer for valuable comments and suggestions. This work was supported by the Czech Science Foundation and Deutsche Forschungsgemeinschaft under the common grant 18-08097J – DE 787/5-1 and the institutional support RVO:67985815 of the Czech Academy of Sciences. The Dunn Solar Telescope was run by the National Solar Observatory (NSO), which is operated by the Association of Univer-

sities for Research in Astronomy, Inc. (AURA), for the National Science Foundation. IBIS has been built by INAF/Osservatorio Astrofisico di Arcetri with contributions from the Universities of Firenze and Roma “Tor Vergata”, NSO, and the Italian Ministries of Research (MIUR) and Foreign Affairs (MAE). The observations at IBIS were supported by the Rome Tor Vergata “Innovative techniques and technologies for the study of the solar magnetism” grant funded by MIUR.

## REFERENCES

- Avrett, E. H. 1981, in NATO ASIC Proc. 68: Solar Phenomena in Stars and Stellar Systems, ed. R. M. Bonnet & A. K. Dupree, 173–198
- Bel, N., & Leroy, B. 1977, *A&A*, 55, 239
- Bello González, N., Flores Soriano, M., Kneer, F., & Okunev, O. 2009, *A&A*, 508, 941, doi: [10.1051/0004-6361/200912275](https://doi.org/10.1051/0004-6361/200912275)
- Cauzzi, G., Reardon, K. P., Uitenbroek, H., et al. 2008, *A&A*, 480, 515, doi: [10.1051/0004-6361:20078642](https://doi.org/10.1051/0004-6361:20078642)
- Cavallini, F. 2006, *SoPh*, 236, 415, doi: [10.1007/s11207-006-0103-8](https://doi.org/10.1007/s11207-006-0103-8)
- Heinzel, P., & Štěpán, J. 2019, in *Astronomical Society of the Pacific Conference Series*, Vol. 519, *Astronomical Society of the Pacific Conference Series*, ed. K. Werner, C. Stehle, T. Rauch, & T. Lanz, 59
- Jefferies, S. M., Fleck, B., Murphy, N., & Berrilli, F. 2019, *ApJL*, 884, L8, doi: [10.3847/2041-8213/ab4719](https://doi.org/10.3847/2041-8213/ab4719)
- Jefferies, S. M., McIntosh, S. W., Armstrong, J. D., et al. 2006, *ApJL*, 648, L151, doi: [10.1086/508165](https://doi.org/10.1086/508165)
- Jess, D. B., Morton, R. J., Verth, G., et al. 2015, *SSRv*, 190, 103, doi: [10.1007/s11214-015-0141-3](https://doi.org/10.1007/s11214-015-0141-3)
- Khomenko, E. 2009, in *Astronomical Society of the Pacific Conference Series*, Vol. 416, *Solar-Stellar Dynamos as Revealed by Helio- and Asteroseismology: GONG 2008/SOHO 21*, ed. M. Dikpati, T. Arentoft, I. González Hernández, C. Lindsey, & F. Hill, 31, <https://arxiv.org/abs/0812.0040>
- Khomenko, E., & Cally, P. S. 2012, *ApJ*, 746, 68, doi: [10.1088/0004-637X/746/1/68](https://doi.org/10.1088/0004-637X/746/1/68)
- Leka, K. D., Barnes, G., & Crouch, A. 2009, in *Astronomical Society of the Pacific Conference Series*, Vol. 415, *The Second Hinode Science Meeting: Beyond Discovery-Toward Understanding*, ed. B. Lites, M. Cheung, T. Magara, J. Mariska, & K. Reeves, 365
- Lites, B. W., Low, B. C., Martinez Pillet, V., et al. 1995, *ApJ*, 446, 877, doi: [10.1086/175845](https://doi.org/10.1086/175845)
- Pesnell, W. D., Thompson, B. J., & Chamberlin, P. C. 2012, *SoPh*, 275, 3, doi: [10.1007/s11207-011-9841-3](https://doi.org/10.1007/s11207-011-9841-3)
- Rajaguru, S. P., Sangeetha, C. R., & Tripathi, D. 2019, *ApJ*, 871, 155, doi: [10.3847/1538-4357/aaf883](https://doi.org/10.3847/1538-4357/aaf883)
- Ruiz Cobo, B., & del Toro Iniesta, J. C. 1992, *ApJ*, 398, 375, doi: [10.1086/171862](https://doi.org/10.1086/171862)
- Rybicki, G. B., & Hummer, D. G. 1991, *A&A*, 245, 171
- . 1992, *A&A*, 262, 209
- Sobotka, M., Del Moro, D., Jurčák, J., & Berrilli, F. 2012, *A&A*, 537, A85, doi: [10.1051/0004-6361/201117851](https://doi.org/10.1051/0004-6361/201117851)
- Sobotka, M., Heinzel, P., Švanda, M., et al. 2016, *ApJ*, 826, 49, doi: [10.3847/0004-637X/826/1/49](https://doi.org/10.3847/0004-637X/826/1/49)
- Sobotka, M., Švanda, M., Jurčák, J., et al. 2013, *A&A*, 560, A84, doi: [10.1051/0004-6361/201322148](https://doi.org/10.1051/0004-6361/201322148)
- Stangalini, M., Del Moro, D., Berrilli, F., & Jefferies, S. M. 2011, *A&A*, 534, A65, doi: [10.1051/0004-6361/201117356](https://doi.org/10.1051/0004-6361/201117356)
- Vecchio, A., Cauzzi, G., Reardon, K. P., Janssen, K., & Rimmele, T. 2007, *A&A*, 461, L1, doi: [10.1051/0004-6361:20066415](https://doi.org/10.1051/0004-6361:20066415)
- Vernazza, J. E., Avrett, E. H., & Loeser, R. 1981, *ApJS*, 45, 635, doi: [10.1086/190731](https://doi.org/10.1086/190731)
- Withbroe, G. L., & Noyes, R. W. 1977, *ARA&A*, 15, 363, doi: [10.1146/annurev.aa.15.090177.002051](https://doi.org/10.1146/annurev.aa.15.090177.002051)